

Catastrophic vs Gradual Collapse of Thin-Walled Nanocrystalline Ni Hollow Cylinders As Building Blocks of Microlattice Structures

Jie Lian,^{*,†} Dongchan Jang,[†] Lorenzo Valdevit,[‡] Tobias A. Schaedler,[§] Alan J. Jacobsen,[§] William B. Carter,[§] and Julia R. Greer[†]

[†]Division of Engineering and Applied Sciences, California Institute of Technology, 1200 East California Boulevard, MC 309-81, Pasadena, California 91125-8100, United States

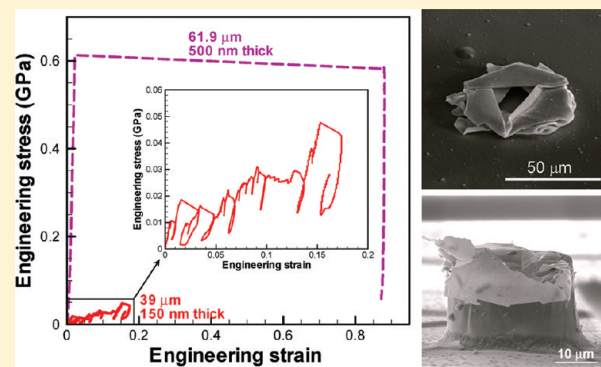
[‡]Department of Mechanical and Aerospace Engineering, University of California, 4227 Engineering Gateway, Irvine, California 92697-3975, United States

[§]Sensors and Materials Laboratory, HRL Laboratories LLC, 3011 Malibu Canyon Road, Malibu, California 90265-4797, United States

 Supporting Information

ABSTRACT: Lightweight yet stiff and strong lattice structures are attractive for various engineering applications, such as cores of sandwich shells and components designed for impact mitigation. Recent breakthroughs in manufacturing enable efficient fabrication of hierarchically architected microlattices, with dimensional control spanning seven orders of magnitude in length scale. These materials have the potential to exploit desirable nanoscale-size effects in a macroscopic structure, as long as their mechanical behavior at each appropriate scale — nano, micro, and macro levels — is properly understood. In this letter, we report the nanomechanical response of individual microlattice members. We show that hollow nanocrystalline Ni cylinders differing only in wall thicknesses, 500 and 150 nm, exhibit strikingly different collapse modes: the 500 nm sample collapses in a brittle manner, via a single strain burst, while the 150 nm sample shows a gradual collapse, via a series of small and discrete strain bursts. Further, compressive strength in 150 nm sample is 99.2% lower than predicted by shell buckling theory, likely due to localized buckling and fracture events observed during *in situ* compression experiments. We attribute this difference to the size-induced transition in deformation behavior, unique to nanoscale, and discuss it in the framework of “size effects” in crystalline strength.

KEYWORDS: Nanocrystalline Ni, shell collapse, uniaxial compression, buckling strength, microlattice structures



Lightweight cellular materials, like foams, honeycombs, and lattice structures, often possess enhanced thermal, mechanical, and energy absorbing properties, far beyond those of their solid counterparts. As such, they have been used in many engineering structures, for example, as cores for stiff, strong, and lightweight sandwich shells and as components designed for impact mitigation in automotive, aerospace, and railway applications. In contrast to random-cell materials (stochastic foams), ordered cellular structures (lattice materials) exhibit enhanced stiffness and strength per unit mass. These benefits arise due to a key difference in their deformation modes: while stochastic foams deform via wall bending mechanisms, ordered lattice structures can be designed to deform by stretch-dominated mechanisms (i.e., tension and compression in the members). The implication is that in topologically designed lattices, stiffness and strength scale linearly with relative density, in contrast with 1.5–2.0 power laws for stochastic foams, with substantial increases in specific stiffness, strength, and energy absorption, particularly at low relative densities.^{1,2} These attributes make lattices ideal for several applications, for example, for cores of

sandwich structures.^{3–7} However, in many applications, current lattice fabrication techniques are generally capable of producing only “large” cell sizes, on the centimeter or possibly millimeter scale.⁸ Resulting properties of such macroscale lattices are well described using traditional solid mechanics principles. With the advent of advanced micro- and nanofabrication techniques, it has now become possible to create macroscopic lattice geometry structures⁹ with controllable nanoscale dimensions, as shown in Figure 1, thereby enabling exploitation of new mechanical behavior that can arise at the nanoscale.¹⁰ It has been shown, for example, that at the nanometer scale, the ductility of a generally brittle polymer photoresist can be enhanced by 300% when the material is patterned into a microlattice architecture,¹¹ that single-crystalline metals get stronger,¹² and that metallic glasses undergo a transition from brittle failure to homogeneous extension.¹³ By utilizing polymer microlattice structures with

Received: May 31, 2011

Revised: August 12, 2011

Published: August 18, 2011

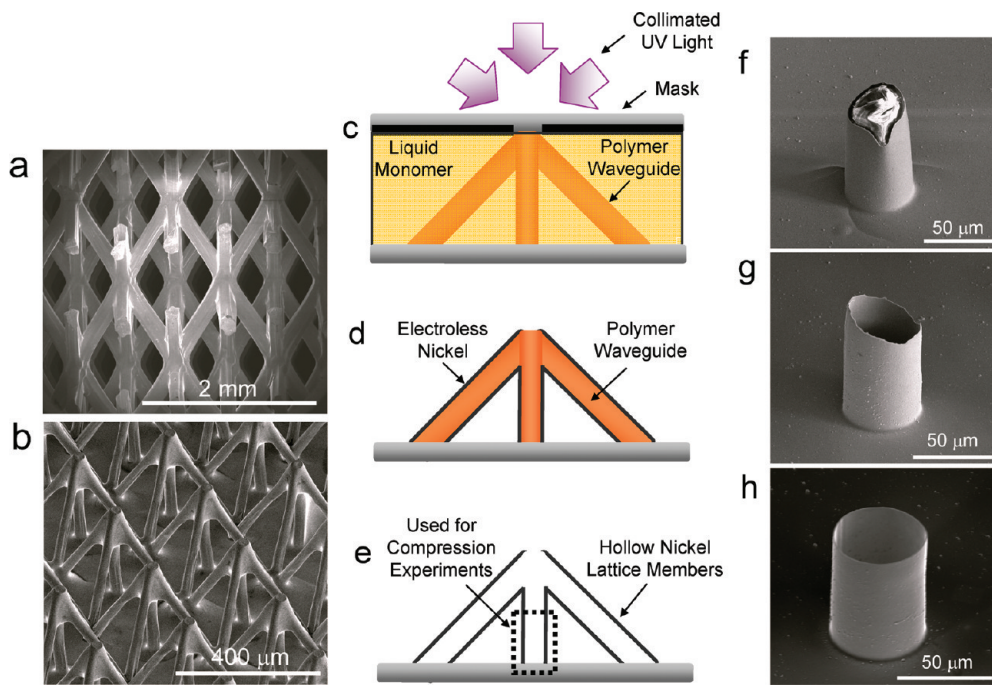


Figure 1. Fabrication processes of vertically oriented hollow Ni cylinder. (a) SEM image of planar view of microlattice. (b) SEM image of Ni plated microlattice structure with angled and vertical lattice members. (c) A schematic of the setup used to fabricate angled and vertical polymer microlattice members. (d) After exposure and removal of the excess liquid monomer, the polymer microlattice members were plated with electroless Ni 500 nm thick. (e) The polymer template was removed with 3 M NaOH, resulting in hollow Ni microlattice members. (f–h) SEM image of a single microlattice member with polymer still inside (f), after etching the polymer (g), and after planarizing the top via FIB revealing nearly perfect cylindrical shape (h).

diameters of truss members less than $100 \mu\text{m}$ as templates for electroless deposition, it is possible to form metallic microlattice structures where the truss member wall thickness (Figure 1h) is in the nanoscale regime. Thus, the truss member's wall thickness becomes comparable to the material's characteristic microstructural dimensions. Under such conditions, interactions between the limiting external dimensions, i.e., truss wall thickness, and the microstructural parameter, i.e. grain size, can drastically alter mechanical strength, as has been shown for a large variety of small-scale metallic structures.^{12,14–16} However, in lattice-type structures, a wider range of interactions must be considered: wall thickness, orientation of free surfaces to loading direction, and film curvature. The resulting mechanical implications at the macroscale are not readily determined. As a result, in order to capitalize on size-dependent mechanical properties in a three-dimensional lattice structure, developing a thorough understanding of the interplay between geometry, microstructure, and reduced dimensions is of paramount importance.

In this work, we report the compressive behavior of vertically oriented, individual microlattice truss members (Figure 1h) with submicrometer-sized wall thicknesses from a nickel microlattice structure. Although these types of thin-shell buckling problems are not new, all previous studies were carried out at a significantly larger scale, with lowest wall thicknesses reported on the order of millimeters.^{17,18} In contrast with the typical smooth compressive behavior of such macroscale cylindrical shells, here we observe a buckling response that is rapid and discrete, with a high thickness-dependent deformation morphology. The samples studied here are at least three orders of magnitude smaller than ever studied before and, most importantly, comparable with critical microstructural material dimensions, i.e. grain size. The wall thicknesses in our nanocrystalline Ni samples are 500 nm (thick series) and 150 nm (thin series), respectively, with an average

grain size of $6.6 \text{ nm} \pm 2.4 \text{ nm}$, as shown in the grain size distribution histogram in Figure 2c. Notably, the only significant difference between these two sets of samples is the cylinder wall thickness, as they were prepared by the same electroless plating process for different time durations, resulting in identical internal microstructure. We find that the collapse strength of thick samples is in good agreement with finite elements calculations (details below), whereas the thin samples are 99.2% lower than the analytically predicted strength and 73.7% weaker than finite element calculations. By concurrently analyzing in situ scanning electron microscopy (SEM) compression movies and mechanical data provided in Supporting Information as well as post-mortem SEM images, we find that the collapse modes of thick and thin samples are quite distinct: a single rapid collapse with no plasticity occurring before failure in the former, while a series of very short bursts with notable localized plasticity and fracture events occurs in the latter. The most important factor appears to be the reduced critical length scale in both the microstructure (i.e., nanometer-scale grain size) and the sample geometry (i.e., wall thickness) that give rise to this previously unobserved signature of cylinder collapse. We discuss these mechanical results and morphological evolution in the framework of microstructural analysis, nano-mechanical testing, and finite element modeling.

Nickel hollow-cylinder lattice members were fabricated and tested for this study to represent the individual structural elements of a three-dimensional lightweight microlattice structure, as shown in Figure 1b. This particular microlattice structure includes a single layer unit cell with both angled and vertical microlattice members. Fabrication of nickel hollow cylinder microlattice structures began with the fabrication of a polymer template formed from a pattern of self-propagating photopolymer waveguides.⁹ Briefly, the process involves placing a mask with a square pattern of circular apertures

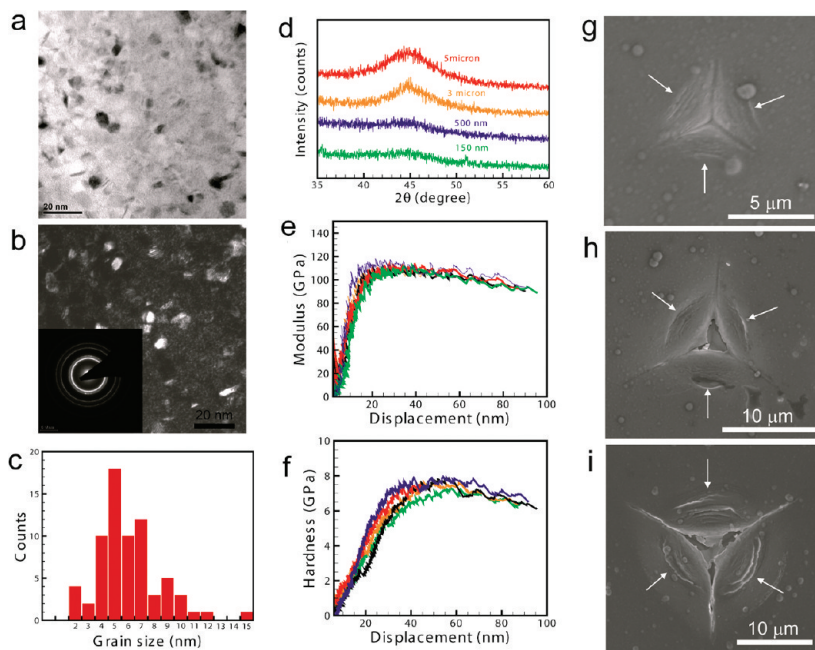


Figure 2. Microstructural and mechanical characterization of electroless Ni films. (a, b) TEM images of the nanocrystalline Ni film prepared by electroless deposition in (a) bright and (b) dark fields. A selected area diffraction pattern is shown in the corner of (b). (c) Histogram of grain size. (d) XRD pattern of electroless Ni films with thicknesses of 5 and 3 μm and 500 and 150 nm. (e) Elastic modulus and (f) hardness vs displacement for nanoindentation into the 1 nm grained electroless Ni film measured from 5 indentation tests. (g–i) SEM images of residual indentations in the 6.6 nm grained electroless Ni film with indentation depth of (g) 200 nm, (h) 500 nm, and (i) 2 μm .

over a volume of photomonomer. The mask is exposed simultaneously to five collimated UV beams generated by a mercury arc lamp. Four of the collimated beams have a 40° equal incident angle off the mask surface but are rotated 90° about the mask normal. A fifth beam is directed normal to the mask surface, resulting in a vertical lattice member, as shown in Figure 1c–e. The height of the repeating unit cell, shown in Figure 1a, is controlled by containing the photomonomer in a volume with a depth corresponding to the first waveguide nodal connection point below the mask surface. Further details regarding the polymer microlattice fabrication process can be found in refs 19 and 20.

Nickel microlattice samples were fabricated by conformally depositing a thin layer of nickel–phosphorus on the polymer templates described above using a commercially available electroless deposition process (OM Group Inc., Cleveland, OH). Prior to electroless plating, all samples were thermally postcured at 120°C in air for 12 hours. To prepare the surface for electroless plating, the samples were first immersed in chromic acid, followed by palladium catalyst activator and acid accelerator (Fidelity 1018 and 1019, OM Group Inc.). The samples were then immersed in electroless nickel plating solution (9026M, OM Group Inc.) and held at 80°C . To achieve different film thicknesses, samples were plated for 1 min to produce the 150 nm-thick films and for 3 min to produce the 500 nm-thick films while maintaining all other parameters constant. The autocatalytic reaction during electroless plating ensured uniform, conformal coating of the complex-shaped, nonplanar sample surface. The reaction involved sodium hypophosphite as a reducing agent, and the resulting deposit contained 7 wt % phosphorus. After nickel deposition, the top surface of the sample was sanded to expose the polymer inner core, which was subsequently removed by submerging the samples in 3 M NaOH at 60°C for 12 h. Transmission electron microscopy

(TEM), X-ray diffraction (XRD), and energy-dispersive spectroscopy (EDS) analyses reveal that the microstructure, i.e. grain size, distribution, and P content, is nearly equivalent in samples of both thicknesses, and hereafter, the deposited Ni–P thin films of all thicknesses are referred to as “electroless nickel films”.

To investigate the mechanical behavior of individual truss members, free-standing vertical polymer lattice members were produced on glass substrates by removing the angled collimated beams during the exposure process described above. The individual polymer lattice members were subsequently electrolessly plated, as shown in Figure 1f. Removal of the polymer (Figure 1g) created the hollow cylinder nickel microlattice members used for uniaxial compression testing. The initially rough top cylinder surfaces were planarized using a focused ion beam (FIB), yielding a nearly perfect cylindrical shell shape, as shown in Figure 1h.

To assess the microstructure of the electroless nickel films, 5 μm -thick samples for TEM microstructural analysis were prepared by a now-standard liftout procedure²¹ via an Omniprobe manipulator inside of a FIB FEI Nova 600. The grain texture of these films was also characterized by XRD. A Bruker AXS D8 advanced X-ray diffractometer with Cu $\text{K}\alpha 1$ implement radiation was used for XRD measurement. The X-ray wavelength is 1.540598 Å for Cu $\text{K}\alpha 1$. All scans were taken in continuous mode for a 2θ range of 35 – 60° . Figure 2 shows several through the thickness TEM images of a 5 μm -thick electroless Ni film. Figure 2a,b shows the bright field (BF) and dark field (DF) TEM images of the cross-sectional Ni film microstructure. Grain sizes were determined by matching the total of 70 grains from 5 different DF images to circles of equivalent area. The mean grain size was found to be 6.6 nm, with the standard deviation of 2.4 nm and the median of 6.1 nm, indicating a tight and self-consistent grain size distribution. To characterize the grain size with an independent technique, XRD spectra generated for 5

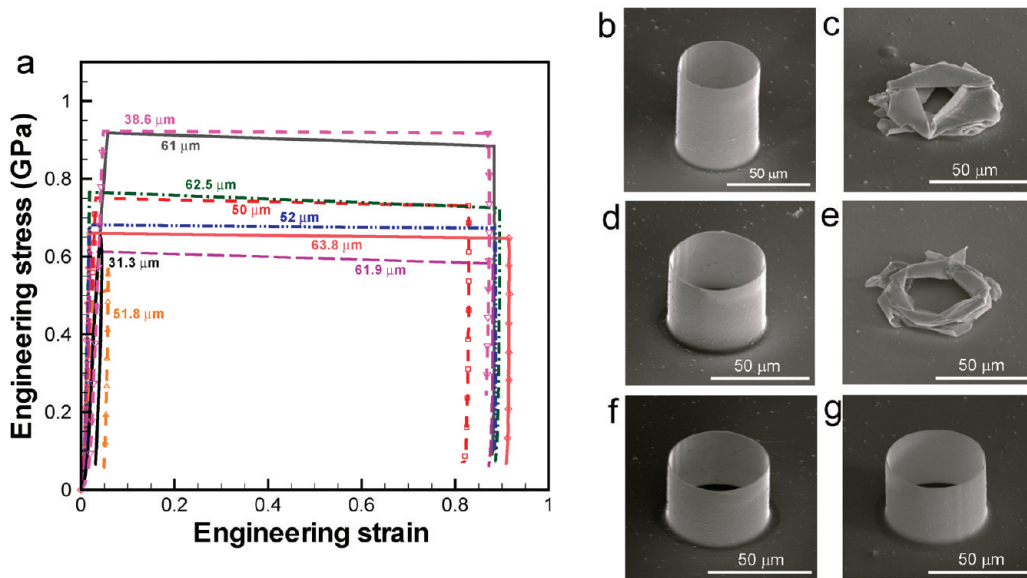


Figure 3. Uniaxial compression results for the 500 nm-thick vertically oriented hollow Ni cylinder. (a) Engineering stress–strain curves of compression of different hollow cylinders with a high displacement rate of 50 nm/s. (b, c) SEM images of 500 nm thick hollow cylinder with height of 62 μm before (b) and after (c) the compression. (d, e) SEM images of 500 nm thick hollow cylinder with height of 39 μm before (d) and after (e) the compression. (f, g) SEM images of 500 nm thick hollow cylinder with height of 31 μm before (f) and after (g) the compression.

and 3 μm - and 500 and 150 nm-thick films are shown in Figure 2d. Applying the Scherrer model to the X-ray spectra:²²

$$G = \frac{K\lambda}{L \cos \theta} \quad (1)$$

where $K = 0.94$ is the Scherrer constant, $\lambda = 1.540598 \text{ \AA}$ is the X-ray wavelength, β is full width at half-maximum (fwhm) of the peak, and θ is Bragg's angle, and the grain size was calculated to be 3–4 nm, which is in agreement with that determined from TEM analysis within experimental error. The electron diffraction pattern (Figure 2b) and the XRD spectra (Figure 2d) clearly reveal the nanocrystalline nature of these Ni films and confirm that the average grain size does not change significantly with film thickness for the film thicknesses studied. The phosphorus content in our Ni films was found to be 7 wt % as measured via EDS and appears to be consistent with that reported in literature on nanocrystalline Ni thin films produced by similar electroless plating techniques.^{23–25}

To gain insights into some aspects of mechanical properties of nanocrystalline Ni, flat electroless Ni thin films deposited on Si substrates were characterized by nanoindentation. Figure 2d shows the elastic modulus increasing up to its maximum value of 110 GPa at 20 nm indentation depth with the concurrent increase in hardness up to 8 GPa (Figure 2e) in the elastic range, with both slightly decreasing with increasing contact depth due to the substrate effect. To minimize interference from the substrate, the indentation depth did not exceed 10% of the film thickness. We estimate average elastic modulus to be 102 ± 10.2 GPa and hardness to be 6.3 ± 0.4 GPa, both calculated at contact depths between 40 and 80 nm. These findings are in reasonable agreement with previously reported values for nanocrystalline Ni with similar grain sizes, with modulus varying from 50 to 168 GPa and hardness from 4.9 to 8.2 GPa.^{26,27} The relatively wide ranges of modulus and hardness reported previously stem from their sensitivity to pH of plating solution and weight fraction of phosphorus.²⁶ For example, Chang et al.

reported elastic modulus of 146 GPa and hardness of 6.1 GPa for Ni–P films deposited at pH of 3.75 and 12 wt % P, while those deposited at pH of 6.0 and 9 wt % P increased to 168 and 8.2 GPa, respectively.²⁶

Nanoindentation into electroless Ni thin films further corroborated their nanocrystalline microstructure. Typically, plastic deformation of nanocrystalline metals does not occur homogeneously, as is the case with their larger grained counterparts. At grain sizes of a few nanometers, several metals exhibit glass-like behavior, manifested by formation of highly localized shear bands.²⁸ Indeed, SEM images of residual nanoindentation marks made in our electroless Ni films reveal clear shear bands formed around the indents performed at three different depths (Figure 2g–i). Further, radial cracks formed in deeper intents, i.e., 2 μm , revealing the material's propensity for brittle failure.

Next, we investigated the uniaxial compression response of hollow Ni cylinders with 2 different wall thicknesses: 500 nm (thick) and 150 nm (thin). The 500 nm, thick hollow cylinders were uniaxially compressed at two different strain rates, 1.0×10^{-3} and $2.5 \times 10^{-4} \text{ s}^{-1}$. Compression depths were controlled to be between 1 and 30 μm . Figure 3a shows 9 engineering stress–strain curves for these samples with data collection rate set at 50 Hz and strain rates at $1.0 \times 10^{-3} \text{ s}^{-1}$. This plot reveals that all samples with heights between 31 and 64 μm exhibit identical deformation behavior: nearly linear elastic deformation up to strains of 4–10%, followed by a single, sudden, and substantial strain burst, suggesting a transition from stable elastic deformation to an instability occurring at the critical buckling stress.¹⁸ In several cases, strain bursts associated with buckling extended to more than 80%, without any noticeable plasticity. Although all tests were programmed for final unload to occur at 50% strain, the strain bursts often resulted in exceeding this value, sometimes compressing the cylinders by as much as 90%. This happened because strain bursts occurred much faster than prescribed displacement rate, resulting in the feedback control mechanism not being able to catch up with the actual deformation

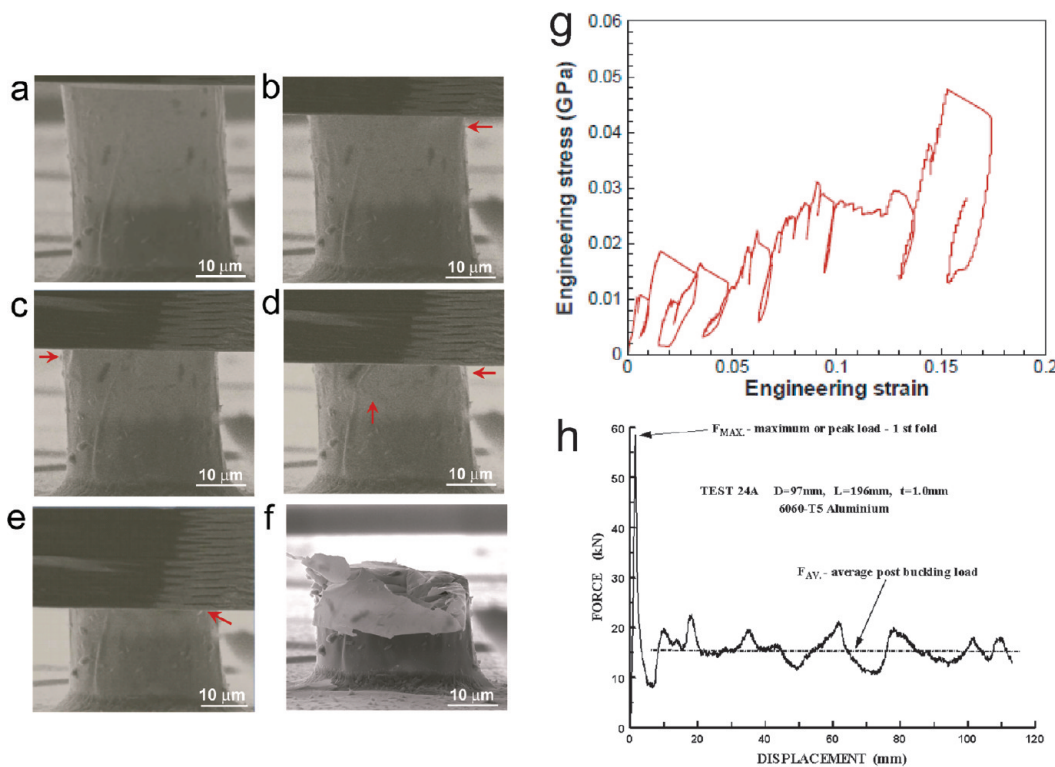


Figure 4. Uniaxial compression results of 150 nm-thick vertically oriented hollow Ni cylinder. (a–f) In situ time progression taken during the compression. (a) Hollow Ni cylinder before compression. (b–e) Local buckles as pointed by red arrows. (f) Hollow Ni cylinder after compression, showing nonaxisymmetric pattern of deformation. (g) Engineering stress–strain curve for uniaxial compression of the 150 nm-thick hollow cylinder. (h) Load–displacement curve for an axially loaded thin-walled metal tube with wall thickness on the order of millimeters. Reprinted with permission from ref 30.

speed. Some samples were intentionally unloaded after compressing by only $1.3\text{--}3\ \mu\text{m}$, corresponding to a strain of 1.7%, to study morphology and mechanical response of the structure prior to its collapse. The similarity between pre- and postdeformation SEM images (Figure 3f,g) and the lack of hysteresis in stress–strain curves suggest that deformation at these small displacements was indeed elastic. An elastic modulus of $\sim 210\ \text{GPa}$ was extracted from the unloading portions of compressive stress–strain curves shown in Figure 3a. This value is more reliable than that measured by nanoindentation ($\sim 102\ \text{GPa}$), since nanoindentation tests are extremely sensitive to surface conditions, and the indentation modulus and hardness could vary with indentation depth due to the highly inhomogeneous flow in nanocrystalline materials.²⁹ Hereafter, the elastic modulus of the electroless Ni film is taken as $210\ \text{GPa}$.

Figure 3(b–e) show pre- and postdeformation images of two representative thick samples with heights of 62 and $39\ \mu\text{m}$. As evidenced from these images, hollow cylinders were completely crushed down, forming polygon topologies and displaying both axial and circumferential wrinkles throughout the structure. Similar geometries have been observed in the axial collapse of macrosized shells and have been referred to as nonsymmetric or “diamond” mode, with a variable number of circumferential lobes or corners.^{17,30} Additional tests on thick hollow cylinders performed at a higher data acquisition rate of $500\ \text{Hz}$ revealed very similar curves (see Figure S1a, Supporting Information), indicating that the strain bursts remained occurred extremely fast, on the order of $10\ \mu\text{s}$. To verify that this strain burst is an intrinsically physical phenomenon rather than an experimental

artifact, displacement vs time curves were also plotted (Figure S2, Supporting Information). Displacement first increases at a constant prescribed rate in the elastic range and then suddenly jumps by $49\ \mu\text{m}$ in $0.012\ \text{s}$, indicating the onset of rapid buckling instability. The presence of several data points captured during the burst indicated that tip and sample remained in contact. Deformation rate during the burst ($\sim 4\ \text{mm/s}$) is 5 orders of magnitude higher than prescribed displacement of $10\ \text{nm/s}$.

Uniaxial compression experiments on 150 nm, thin hollow cylinders were performed in the in situ instrument, SEMentor, allowing capture of real-time videos of their deformation mode. These cylinders were compressed at a constant strain rate of $2.5 \times 10^{-4}\ \text{s}^{-1}$, with a data acquisition rate of $50\ \text{Hz}$. Figure 4a shows a pre-deformation image taken in SEMentor, with diamond flat punch tip in contact with the sample. Figure 4b–e shows a series of sequential frames from the in situ compression movie on a typical thin sample, with Figure 4f showing the structures after final unloading. These figures illustrate that the deformation commenced by localized buckles, as manifested by nonaxisymmetric shrinkage of cylinder walls below the contact region, followed by the development of inward and outward folds and small cracks upon further compression. Figure 4g shows an engineering stress–strain curve corresponding to this compression, which consists of several discrete regions of elastic loading followed by abrupt, short strain bursts, critical stress drops, and reloading segments. This stress–strain signature is markedly different from the elastic-loading single burst-unloading characteristics of uniaxial compressions of 500 nm, thick hollow cylinders.

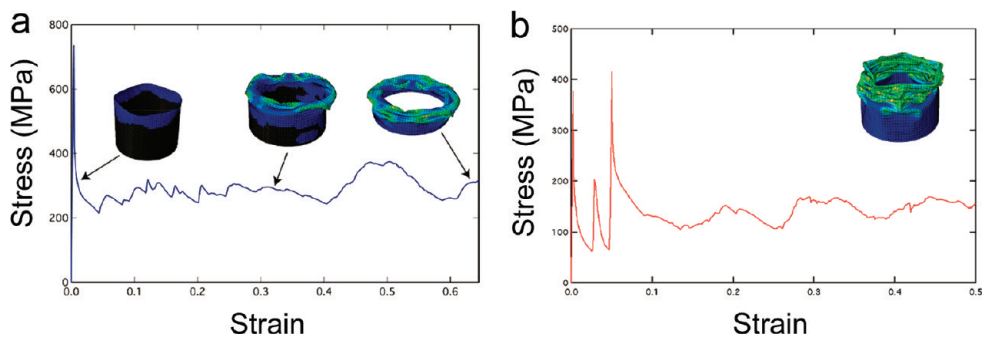


Figure 5. FE analyses results of the uniaxial compression of hollow Ni cylinder. (a, b) Load–displacement curve and geometrical change of the dynamic uniaxial compression of 500 nm-thick hollow cylinder (a) and 150 nm-thick hollow cylinder (b).

To gain further insights into hollow cylinder deformation, stress–strain behavior was correlated with concurrent *in situ* images during compression. We find that stress builds up linearly until the onset of the initial elastic instability, after which an abrupt incremental shortening of the sample is observed. This leads to a sudden strain burst, similar to that observed in the compressions of 500 nm thick samples but significantly shorter. Even during these relatively short strain bursts, the cylinder collapses faster than prescribed displacement rate, leading to a load drop as the nanoindenter tries to maintain constant strain rate followed by elastic reloading, a signature ubiquitously present in the uniaxial compression experiments on micro- and nanopillars.^{12,31,32} Each burst is associated with localized buckling or fracture of a small portion of the cylinder in the vicinity of the contact region, with the bulk of the structure remaining undeformed.

The critical buckling stress and collapse mode are further interpreted in the context of elastic shell buckling and finite elements (FE) analyses. Assuming that a clamped–clamped thin-walled cylinder is stubby enough to prevent Euler (global) buckling, the buckling mode is local, with critical stress given by¹⁸

$$\sigma_{\text{cr}} = \frac{E}{\sqrt{3(1-\nu^2)}} \left(\frac{t}{R} \right) \quad (2)$$

where E and ν are the Young's modulus and Poisson's ratio of (isotropic) material, respectively, t is the wall thickness, and R is cylinder radius. Using the experimentally measured modulus, $E = 210$ GPa and assuming a Poisson's ratio of 0.31, we calculate the stress to be 2.2–3.4 GPa for 500 nm-thick hollow cylinder and ~1.28 GPa for 150 nm-thick sample. Based on experimentally obtained stress–strain curves shown in Figures 3a and 4g, the critical buckling stress can be extracted at the transition point from nearly elastic deformation to the sudden and substantial strain burst. We find the critical buckling stress of 500 nm-thick cylinders to be 0.6–0.95 GPa, whereas that of 150 nm-thick cylinders only ~0.01 GPa. Evidently, theoretical predictions for critical buckling stress of the thick samples are ~2.3–5.7 times higher than experimental values. This discrepancy can be attributed to the difference in boundary conditions (eq 2 pertains to clamped–clamped cylinders, whereas the experimental configuration has a free end) and the possible presence of imperfections. FE simulations, performed with the same boundary conditions as in the experiment and with intentionally embedded imperfections, support this interpretation (Figure 5a), as they agree with experimentally measured critical strength within ~20%. This gap could be further reduced with a more thorough

imperfection sensitivity analysis, which is outside the scope of this report.

In contrast to this relatively marginal difference in computed vs experimental stress levels for the thick samples, eq 2 over-predicts the strength of the thin cylinders by 99.2%. FE simulations do not improve the agreement significantly (measured values of strength remain ~73.7% lower than FE predictions), indicating that the difference cannot be attributed merely to boundary conditions and geometric imperfections. Our *in situ* experiments on the thinner samples reveal that several localized fracture events at the interface between cylinder top and indenter tip occur under axial compression at stresses 2–3 times lower than critical buckling strength (Figure 4). Following such localized fractures, wall ligaments can bend upon themselves, ultimately generating the post-mortem configuration observed experimentally (Figure 4). Therefore, the implementation of localized fracture events in FE simulations may be crucial to capture this behavior.

Further, both FE and analytical approaches are inherently based on a continuum framework, which does not incorporate size-dependent material properties. Yet, when the microstructural length scale is reduced to nanometer dimensions, as is the case with nanograined metals, materials often deform via novel mechanisms, such as grain boundary-assisted plasticity, giving rise to nonbulk-like mechanical behavior, which cannot be captured by classical models.^{33–41} Clearly, the specific microstructural attributes in our 6.6 nm-grained Ni films present a governing factor in explaining the deviation of hollow cylinder deformation from continuum-based predictions.

In the last ~5 years it has been unambiguously demonstrated that nanosized materials, with geometric dimensions comparable to the characteristic length scale of their microstructure, exhibit unique deformation mechanisms, resulting in markedly different mechanical properties, the presence of a “size effect,” and failure by discrete plasticity.⁴¹ For example, Jang and Greer reported that a reduction in external dimensions of 60 nm-grained nanocrystalline Ni to nanometer scale resulted in a “smaller is weaker” phenomenon, whereby 100 nm diameter samples are 1.7 times weaker in compression than 2 μm diameter ones.⁴² While the microstructure of both thin and thick samples in our study is identical, it is plausible that the conspicuously reduced compressive strengths and emergence of ductility in our 150 nm thick hollow cylinders as compared with 500 nm-thick ones can, at least in part, be attributed to the emergence of such a size effect. In order to accurately capture the uniaxial collapse of this thin-walled nanocrystalline Ni hollow cylinder by FE simulations, the implementation of fracture, and brittleness as well as size-dependent material properties are of critical importance.

In addition to the strikingly different compressive strength of the thick and thin samples, their compression behavior is also quite different: the 500 nm samples collapse all at once, while the 150 nm samples shows gradual deformation. In all 500 nm samples, elastic buckling was followed by substantial irrecoverable deformation and crack propagation, and post-mortem samples were completely crushed down, displaying a nonaxisymmetric diamond-like shape. While such post-mortem topology is similar to the diamond collapse shape reported in literature for aluminum alloys,^{17,30} sudden collapse of the entire structure at nearly constant load has not been observed before in metallic shells. We hypothesize that this sudden collapse arises from the brittle deformation nature of our nanocrystalline Ni films, which deformed via forming cracks and localized shear bands when indented, exhibiting limited ductility (Figure 2f–h).

In contrast with the thick samples, the axial compression of 150 nm, thin samples is characterized by several small strain bursts with a number of local buckling and cracking events occurring throughout the experiment. After the test, these hollow cylinders were not crushed but rather retained their cylindrical geometry, with only the top portion having been plastically deformed. This deformation mode, characterized by nonaxisymmetric sequential folding events originating from the sample top and moving downward with increased loading, accompanied by localized fractures is quite different from published results on millimeter-scale cylindrical shells with no evidence of fracture events.¹⁷ Despite the commonality of the bottom portion of the cylinder remaining undeformed during the compression, stress-strain curves reported in literature¹⁷ and in this study are markedly different: the former always displays a sudden stress drop at the onset of first buckling event, followed by a fairly constant plateau, as shown in Figure 4h. In contrast, here we observe discrete regions of elastic loadings followed by short, abrupt strain bursts, critical stress drops, and reloading segments. Based on these clear distinctions, it can be inferred that in the compression of 150 nm thick cylinders, cracks, and local buckling are formed at an early stage of compression at a stress level much below the buckling stress and thus results in the formation of several folds.

In summary, we investigated deformation of vertically oriented 6.6 nm-grained nanocrystalline Ni hollow cylinders with nanometer-sized wall thicknesses subjected to uniaxial compression. Unlike in all previous reports on structural collapse of shell structures, we find that deformation of these nanocylinders is a strong function of their thickness, dimensions, and material microstructure. We observe distinct differences between the behavior of 500 nm thick and 150 nm thick hollow cylinders: (1) the critical buckling stress is 60–95 times higher in thick hollow cylinders than in thin ones, a difference that cannot be explained based on geometry alone; (2) thick hollow cylinders suddenly collapse at strains as low as 2%, whereas thin hollow cylinders exhibit continuous localized fracture and buckling events, clearly indicating that thickness plays a critical role in defining the deformation mechanism. Preliminary FE analysis is promising as it shows qualitative agreement of deformation behavior in hollow cylinders. We discuss these findings in the context of nanocrystalline Ni mechanical properties and microstructure and in the effect of intrinsic and extrinsic size limitations on strength. Our study reveals that in order to utilize microtruss architectures in structural applications, it is critical to account for the size-dependent mechanical properties and their governing deformation mode.

■ ASSOCIATED CONTENT

S Supporting Information. Descriptions of experimental and numerical methods, uniaxial compression results with a higher data acquisition rate of 500 Hz, displacement vs time curves, and in situ compression movies of 150 nm, thin sample. This material is available free of charge via the Internet at <http://pubs.acs.org>.

■ AUTHOR INFORMATION

Corresponding Author

*Email: jljan@caltech.edu.

■ ACKNOWLEDGMENT

The authors gratefully acknowledge the financial support of DARPA through MCMA program, contract no. W91CRB-10C-0305. The authors are grateful to Emily Warmann for helping on XRD work and Sophia Yang for help with sample fabrication. The authors also gratefully acknowledge helpful discussions with John Hutchinson and Mike Baskes.

■ REFERENCES

- (1) Deshpande, V. S.; Ashby, M. F.; Fleck, N. A. *Acta Mater.* **2001**, *49* (6), 1035–1040.
- (2) Ashby, M. F. *Philos. Trans. R. Soc., A* **2006**, *364* (1838), 15–30.
- (3) Deshpande, V. S.; Fleck, N. A. *Int. J. Solids Struct.* **2001**, *38* (36–37), 6275–6305.
- (4) Hyun, S.; Karlsson, A. M.; Torquato, S.; Evans, A. G. *Int. J. Solids Struct.* **2003**, *40* (25), 6989–6998.
- (5) Queheillalt, D. T.; Wadley, H. N. G. *Mater. Sci. Eng., A* **2005**, *397* (1–2), 132–137.
- (6) Sybeck, D. J.; Wadley, H. N. G. *J. Mater. Res.* **2001**, *16* (3), 890–897.
- (7) Wadley, H. N. G.; Fleck, N. A.; Evans, A. G. *Compos. Sci. Technol.* **2003**, *63* (16), 2331–2343.
- (8) Wadley, H. N. G. *Adv. Eng. Mater.* **2002**, *4* (10), 726–733.
- (9) Jacobsen, A. J.; Barvosa-Carter, W.; Nutt, S. *Adv. Mater.* **2007**, *19* (22), 3892–+.
- (10) Schaedler, T.; Jacobsen, A.; Carter, B. *Private communications* **2011**.
- (11) Jang, J. H.; Ullal, C. K.; Choi, T.; Lemieux, M. C.; Tsukruk, V. V.; Thomas, E. L. *Adv. Mater.* **2006**, *18* (16), 2123–2127.
- (12) Greer, J. R.; De Hosson, J. T. M. *Prog. Mater. Sci.* **2011**, *56* (6), 654–724.
- (13) Jang, D.; Greer, J. R. *Nat. Mater.* **2010**, *9* (3), 215–219.
- (14) Arzt, E. *Acta Mater.* **1998**, *46* (16), 5611–5626.
- (15) Uchic, M. D.; Shade, P. A.; Dimiduk, D. M. *Annu. Rev. Mater. Res.* **2009**, *39*, 361–386.
- (16) Kraft, O.; Gruber, P. A.; Monig, R.; Weygand, D. *Annu. Rev. Mater. Res.* **2011**, *40*, 293–317.
- (17) Andrews, K. R. F.; England, G. L.; Ghani, E. *Int. J. Mech. Sci.* **1983**, *25* (9–10), 687–696.
- (18) Brush, D. O.; Almroth, B. O. *Buckling of bars, plates, and shells*; McGraw-Hill, Inc.: New York, 1975.
- (19) Jacobsen, A. J.; Barvosa-Carter, W.; Nutt, S. *Acta Mater.* **2008**, *56* (11), 2540–2548.
- (20) Jacobsen, A. J.; Barvosa-Carter, W.; Nutt, S. *Acta Mater.* **2007**, *55* (20), 6724–6733.
- (21) Giannuzzi, L. A.; Stevie, F. A. *Micron* **1999**, *30* (3), 197–204.
- (22) Scherrer, P. *Nachr. Ges. Wiss. Goettingen* **1918**, *26*, 98–100.
- (23) Weil, R.; Parker, K. *Electroless Plating: Fundamentals & Applications*; William Andrew Publishing/Noyes: Orlando, FL, 1990; Chapter 4.
- (24) Kumar, P. S.; Nair, P. K. *J. Mater. Process. Technol.* **1996**, *56* (1–4), 511–520.

- (25) Kumar, P. S.; Nair, P. K. *J. Mater. Sci. Lett.* **1994**, *13* (9), 671–674.
- (26) Chang, S. Y.; Lee, Y. S.; Hsiao, H. L.; Chang, T. K. *Metall. Mater. Trans. A* **2006**, *37A* (10), 2939–2945.
- (27) Weil, R.; Lee, J. H.; Kim, I.; Parker, K. *Plat. Surf. Finish.* **1989**, *76* (2), 62–66.
- (28) Trelewicz, J. R.; Schuh, C. A. *Acta Mater.* **2007**, *55* (17), 5948–5958.
- (29) Yang, F.; Geng, K.; Liaw, P. K.; Fan, G.; Choo, H. *Acta Mater.* **2007**, *55* (1), 321–327.
- (30) Guillow, S. R.; Lu, G.; Grzebieta, R. H. *Int. J. Mech. Sci.* **2001**, *43* (9), 2103–2123.
- (31) Greer, J. R.; Oliver, W. C.; Nix, W. D. *Acta Mater.* **2005**, *53* (6), 1821–1830.
- (32) Uchic, M. D.; Dimiduk, D. M.; Florando, J. N.; Nix, W. D. *Science* **2004**, *305* (5686), 986–989.
- (33) Van Swygenhoven, H.; Derlet, P. M. *Phys. Rev. B* **2001**, *64* (22), 224105.
- (34) Shan, Z.; Stach, E. A.; Wiezorek, J. M. K.; Knapp, J. A.; Follstaedt, D. M.; Mao, S. X. *Science* **2004**, *305* (5684), 654–657.
- (35) Van Swygenhoven, H.; Derlet, P. M.; Hasnaoui, A. *Phys. Rev. B* **2002**, *66* (2), 024101.
- (36) Kumar, K. S.; Suresh, S.; Chisholm, M. F.; Horton, J. A.; Wang, P. *Acta Mater.* **2003**, *51* (2), 387–405.
- (37) Gianola, D. S.; Van Petegem, S.; Legros, M.; Brandstetter, S.; Van Swygenhoven, H.; Hemker, K. J. *Acta Mater.* **2006**, *54* (8), 2253–2263.
- (38) Rupert, T. J.; Gianola, D. S.; Gan, Y.; Hemker, K. J. *Science* **2009**, *326* (5960), 1686–1690.
- (39) Chen, M.; Ma, E.; Hemker, K. J.; Sheng, H.; Wang, Y.; Cheng, X. *Science* **2003**, *300* (5623), 1275–1277.
- (40) Ke, M.; Hackney, S. A.; Milligan, W. W.; Aifantis, E. C. *Nanostruct. Mater.* **1995**, *5* (6), 689–697.
- (41) Hemker, K. J. *Science* **2004**, *304* (5668), 221–223.
- (42) Jang, D.; Greer, J. R. *Scr. Mater.* **2011**, *64* (1), 77–80.